AGU PUBLICATIONS

JGR

Journal of Geophysical Research: Space Physics

RESEARCH ARTICLE
10.1002/2017JA024584

Key Points:
- Coseismic deformation reveals the complex mechanism of the Kaikoura earthquake reinforced by differently oriented horizontal displacements
- We demarcate two varying thrust zones resulting from the multislip distributions over the rupture area
- The near-field coseismic ionospheric perturbations are mainly linked to these two surface thrust orientations

Supporting Information:
- Supporting Information S1

Correspondence to:
M. S. Bagiya,
bagiyamala@gmail.com;
mala@iigs.iigm.res.in

Citation:
Bagiya, M. S., Sunil, P. S., Sunil, A. S., & Ramesh, D. S. (2018). Coseismic contortion and coupled nocturnal ionospheric perturbations during 2016 Kaikoura, M_w 7.8 New Zealand earthquake. *Journal of Geophysical Research: Space Physics*, *123*, 1477–1487. https://doi.org/10.1002/2017JA024584

Received 11 JUL 2017
Accepted 21 JAN 2018
Accepted article online 26 JAN 2018
Published online 10 FEB 2018

Coseismic Contortion and Coupled Nocturnal Ionospheric Perturbations During 2016 Kaikoura, M_w 7.8 New Zealand Earthquake

Mala S. Bagiya[1], P. S. Sunil[1], A. S. Sunil[1], and D. S. Ramesh[1]

[1]Indian Institute of Geomagnetism (DST), Navi Mumbai, India

Abstract The oblique-thrust Kaikoura earthquake of M_w 7.8 that struck New Zealand on 13 November 2016 at 11:02:56 UTC (local time at 00:02:56 a.m. on 14 November 2016) was one of the most geometrically and tectonically complex earthquakes recorded onshore in modern seismology. The event ruptured in the region of multisegmented faults and propagated unilaterally northeastward for more than 170 km from the epicenter. The GPS derived coseismic surface displacements reveal a larger widespread horizontal and vertical coseismic surface offsets of ~6 m and ~2 m, respectively, with two distinct tectonic thrust zones. We study the characteristics of coseismic ionospheric perturbations based on tectonic and nontectonic forcing mechanisms and demonstrate that these perturbations are linked to two distinct surface thrust zones with rotating horizontal reinforcement trending the rupture, rather than merely to the displacements oriented along the rupture propagation direction.

Plain Language Summary In general, the Earth crust uplift during any earthquake produces compressional waves in the overlying atmosphere. These waves propagate upward in the region of exponentially decreasing atmospheric neutral density, and thus, its amplitudes increase with atmospheric heights. On arrival at ionospheric heights, the waves redistribute ionospheric electron density and produce electron density perturbations known as coseismic ionospheric perturbations. The thrust earthquakes induce significant crustal uplift, while the strike-slip event mostly deforms the crust horizontally. The massive M_w 7.8 Kaikoura earthquake occurred in the complex multisegmented fault system between the Australia-Pacific plate boundary with a combination of vertical and differently oriented horizontal crust movements. This study reports that the two distinct thrust zones over the rupture area resulted from the uplift with reinforcement of rotating horizontal motion from the epicenter act as key tectonic sources for the peculiar distribution of coseismic ionospheric perturbations around the epicenter.

1. Introduction

The massive M_w 7.8 Kaikoura earthquake occurred in the northern region of the South New Zealand Island on 13 November 2016 at 11:02:56 UTC (local time at 00:02:56 a.m. on 14 November 2016). This is the largest seismic event in New Zealand region since the 3 February 1931, M 7.8 Hawke's Bay earthquake. The Institute of Geological and Nuclear Sciences, New Zealand, recorded the earthquake epicenter at 42.69°S, 173.02°E with a focal depth of ~15 km. The earthquake triggered as a result of shallow oblique-thrust faulting on or near the tectonically active and complex convergent plate boundary between the Australia and Pacific plates. The focal mechanism solution (U.S. Geological Survey, 2016) indicates that the preferred fault plane of the main shock strikes northeast roughly parallel to the coast line with a down-dip toward northwest direction (Figure 1a). The event occurred along the multisegmented fault zones in a combination of differentially oriented thrust as a major component along with strike-slip extending over the rupture length of ~170 km toward northeast from the epicenter (Duputel & Rivera, 2017).

The crustal surface deformation associated with the rupture propagation is considered to be the main energy source that induced ionospheric perturbations (e.g., Heki et al., 2006; Sunil et al., 2016, and references therein). The coseismic surface uplift induces acoustic wave velocity perturbations in the nearby atmosphere, which propagate vertically upward in the region of decreasing neutral density, and thus, their amplitudes increase to conserve the total kinetic energy. Once the velocity perturbations encounter the ionospheric plasma, the ion-neutral collisions redistribute this plasma to manifest as the electron density perturbations which are termed as coseismic ionospheric perturbations (CIP) (e.g., Sunil et al., 2016). The CIP amplitudes

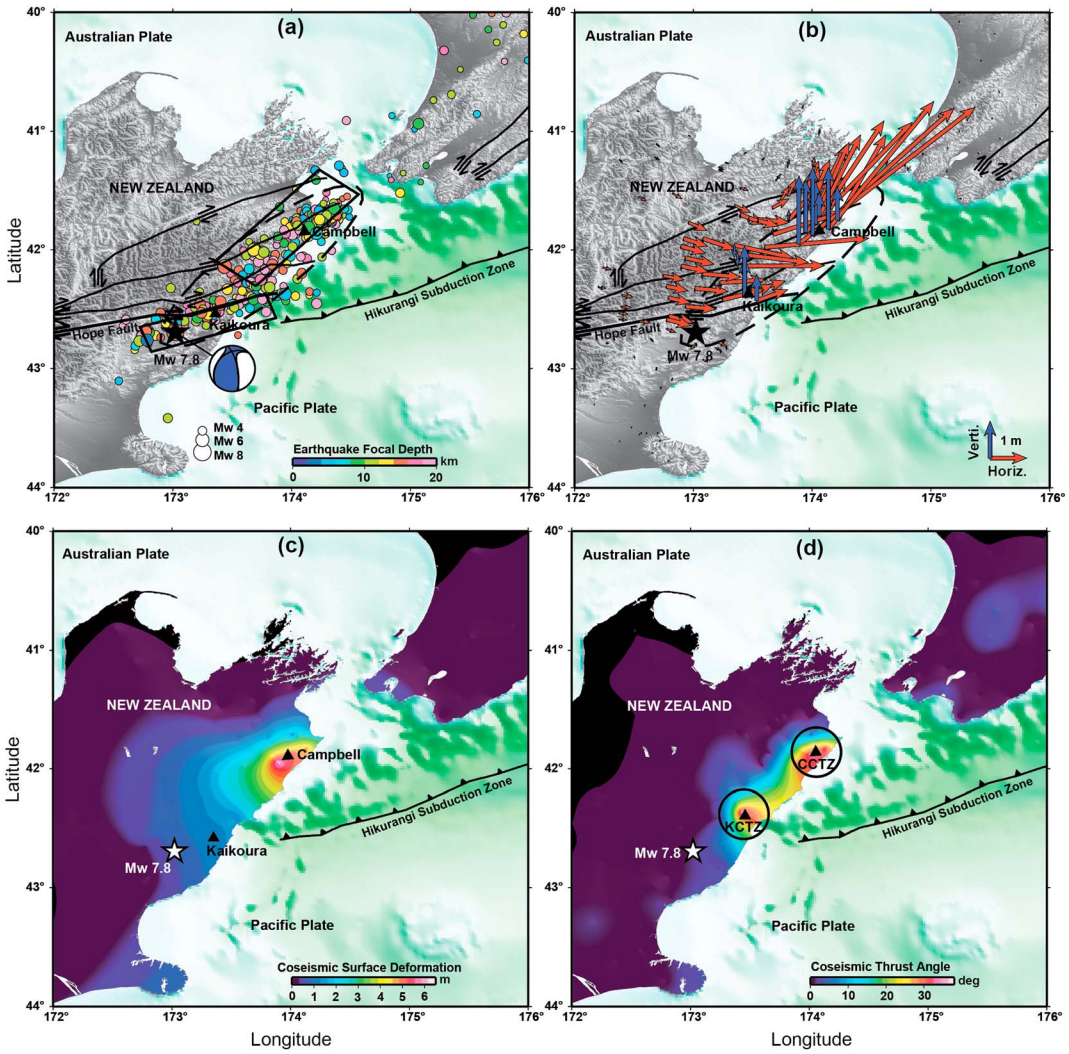

Figure 1. (a) Map represents the epicenter location (black star) of 13 November 2016 (M_w 7.8) Kaikoura earthquake. The aftershocks as a function of depth are presented with colored circles. The size of the circle represents the different magnitudes. The rupture area is highlighted in black dashed ellipse. The beach ball indicates the oblique thrust faulting focal mechanism solution (U.S. Geological Survey 2016). The rectangles represent surface projection of finite fault slip models after Zhang et al. (2017). (b) The blue and red velocity vectors indicate the GPS derived vertical and horizontal coseismic displacements. (c) Relief map of GPS derived coseismic total surface deformation map. (d) Relief map of GPS derived coseismic thrust angle from horizon. The black circles indicate the identified coseismic thrust zones Campbell Coseismic Thrust Zone (CCTZ) and Kaikoura Coseismic Thrust Zone (KCTZ) at Campbell and Kaikoura, respectively.

and phase are mainly controlled by the nontectonic forcing mechanisms of geomagnetic field-wave coupling, satellite geometry at the sounding heights, and ambient ionization density. The azimuthal distribution of near-field CIP, in general, follows rupture propagation if nontectonic forcing mechanisms favor the evolution of the same (e.g., Bagiya et al., 2017; Rolland et al., 2013; Sunil et al., 2016).

Sunil et al. (2016) investigated CIP related to M_w 7.8 Nepal earthquake occurred on 25 April 2015, which is a pure thrust event, and explained the azimuthal propagation of the near-field CIP in terms of rupture direction with respect to the epicentral location. Further, Bagiya et al. (2017) studied the coseismic ionospheric response during the Nepal event of M_w 7.3 on 12 May 2015 and emphasized the role of nontectonic forcing mechanism of satellite geometry in controlling the amplitude distribution of CIP around the epicenter. They have shown that owing to the wave phase cancellation effects during varying satellite geometry, CIP evolved with significantly less amplitudes in southeast direction where basically the rupture propagated. Thus, it

becomes important to evaluate the CIP amplitude distribution in terms of various nontectonic forcing mechanisms, that is, geomagnetic field-acoustic wave coupling, wave phase cancellation effects during varying satellite geometry, and ambient ionization variability, before attributing it to any crustal deformation source pattern. To further validate the azimuthal distribution of CIP in terms of tectonic forcing, the recent Kaikoura earthquake that occurred along multiple faults with differently oriented thrusts serves as one of the best geometrically and tectonically complex examples. In this paper, first, we discuss the Global Positioning System (GPS) derived surface deformation and associated thrust orientations in terms of local complex structure and tectonics. Using the mid nighttime CIP, captured by satellites orbiting in different azimuthal direction, we report that CIP evolution strongly depends on the surface thrust orientations along the rupture direction rather than only on the coseismic displacements along the rupture. In addition, it is suggested that the CIP are mainly induced by the two distinct thrust zones along the rupture during the Kaikoura earthquake. It is therefore proposed that the thrust angles and the successive orientations resulting from the combination of the vertical and the differently oriented horizontal crustal deformation components are the main cause of the observed CIP distribution. The results are discussed in the light of current understanding on the additional effects of nontectonic forcing mechanisms on CIP evolution.

2. Data and Observations

2.1. Coseismic Crustal Deformation Offsets

In the present study, GeoNet and PositioNZ Global Navigation Satellite Systems (GNSS) networks form the main GPS data source to extract information about crustal deformation and the related ionospheric variations. The initial coseismic surface deformation related to M_w 7.8 Kaikoura earthquake is derived from GPS position time series recorded at various continuous GPS sites extended over the northern region of the South New Zealand Island. Initially, common three-dimensional offset (north-south, east-west, and vertical) at the epoch of 13 November 2016 has been estimated in least squares sense by differencing the mean site positions of all available continuous GPS stations near the epicenter. In order to reduce the errors in the position estimation, we have considered the GPS position time series of 5 days before and after the earthquake. The standard deviations of the coseismic offset are estimated depending on the deviation from normality of the detrended residuals (Williams et al., 2004). Additionally, the campaign GPS data from Hamling et al. (2017) are also incorporated for coseismic crustal deformation evaluation.

Figure 1b shows the coseismic horizontal and vertical displacements in red and blue vectors, respectively. The recorded GPS data show that the largest widespread horizontal and vertical coseismic surface offsets are ~6 m and ~2 m, respectively, near Cape Cambpell, located approximately ~110 km northeast of the epicenter. Another discrete zone of horizontal and vertical offsets observed nearby Kaikoura, ~50 km in northeast from the epicenter. Hence, it is interesting to note that the horizontal offset during the Kaikoura event oriented easterly closer to the epicenter first and get amplified further northeast along the rupture with a northerly attitude indicating an anticlockwise rotation from the epicentral region. It is also pertinent to note that though the rupture initiated south of the Hope Fault (Figure 1b), it propagated in northeast direction across the shear zone of complex plate boundary consisting numerous strike-slip faults trending ENE-WSW. To demonstrate the coseismic offset over the rupture area, we derive the total coseismic deformation map (Figure 1c) of the entire area from the horizontal and vertical GPS components and compared with interferometric synthetic aperture radar derived deformation (Hamling et al., 2017). It could be noticed that the GPS derived total displacement field, of present study, shows a good agreement with interferometric synthetic aperture radar observations.

To envisage further, we computed the deformation thrust angle by decomposing horizontal and vertical GPS velocity components. Figure 1d depicts the two distinct coseismic thrust zones Campbell Coseismic Thrust Zone (CCTZ) and Kaikoura Coseismic Thrust Zone (KCTZ) at Cape Campell and Kaikoura regions, respectively. The maximum computed surface thrust angle at CCTZ (~37.5°) well corroborates with the U.S. Geological Survey, 2016, moment tensor dip angle of 38°. The color shade in Figure 1d indicates the coseismic surface thrust angle from the horizon. The coseismic velocity map (Figure 1b) and thrust angle (Figure 1d) map clearly illustrate the involvement of multisegmented fault system with diverse orientations and subsurface slip directions toward the rupture complexities during the Kaikoura earthquake (e.g., Duputel & Rivera, 2017; Hamling et al., 2017; Zhang et al., 2017).

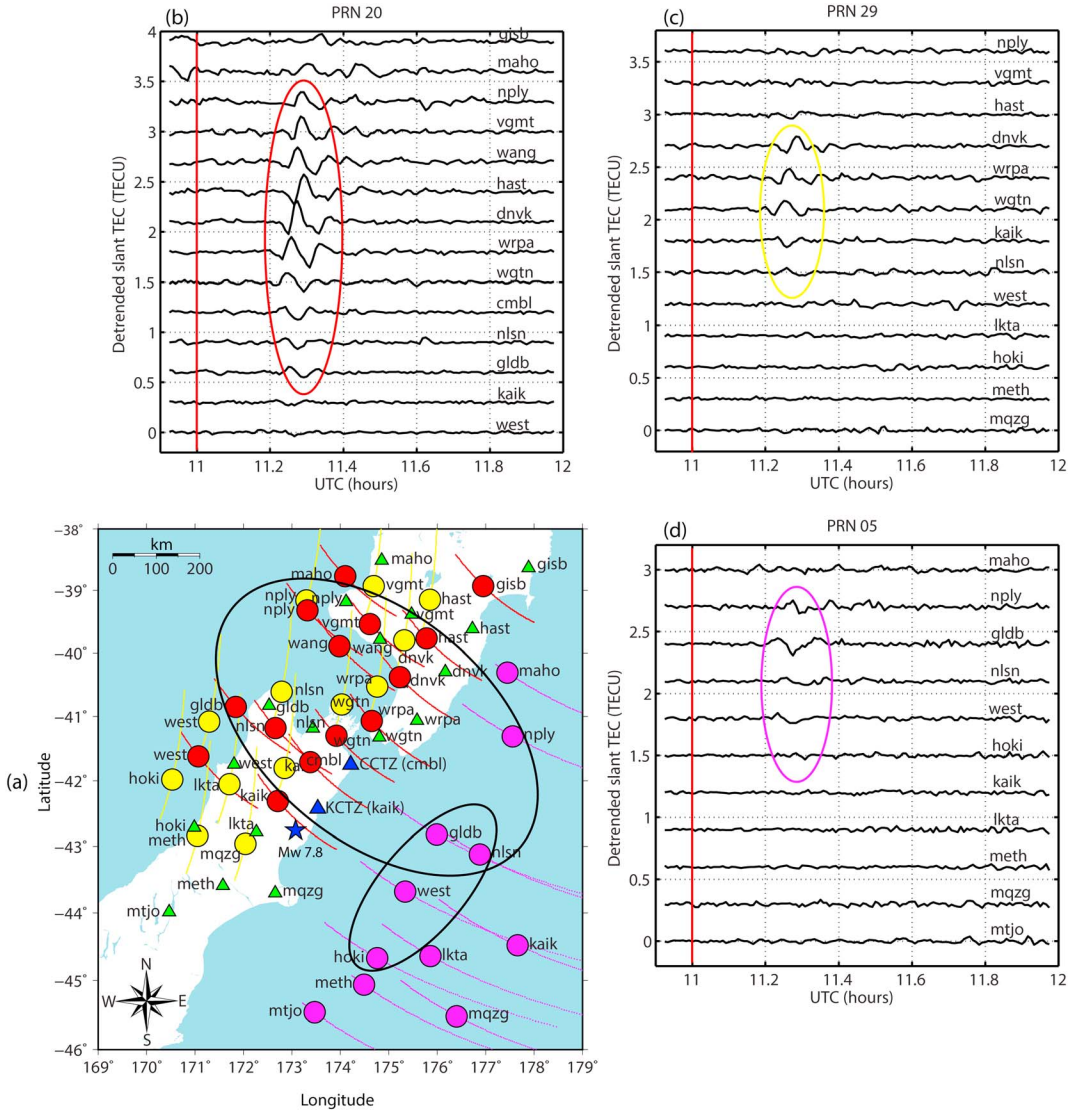

Figure 2. (a) Spatial map illustrating the satellite IPP of PRNs 20 (red), 29 (yellow), and 05 (magenta) at the time of CIP initiation around the rupture zone. Locations of the epicenter, *cmbl* (CCTZ) and *kaik* (KCTZ) GPS sites, are shown in blue. Two highlighted clusters of IPP show the locations where significant CIP are observed. (b) Time series indicating the CIP evolution as observed by PRN 20 around the rupture zone. Significant CIP are highlighted in red ellipse and corresponding northern IPP cluster is represented as red circles in Figure 2a. (c) Same as Figure 2b but for PRN 29. CIP highlighted in yellow ellipse are considered to be significant. Corresponding yellow IPP can be noticed in Figure 2a. (d) Same as Figures 2b and 2c but for PRN 05. Considerable CIP highlighted in magenta ellipse are associated with the north-northeast and southeast magenta IPP cluster in Figure 2a.

2.2. CIP Observations

RINEX GPS observations at every 30 s from all available GPS sites have been used to estimate the slant total electron content. The obtained slant total electron content are detrended further, using the cutoff frequency ≤4.8 mHz, to highlight the desired acoustic wave signals in terms of CIP. It is verified with the World Data Center for Geomagnetism, Kyoto, that there were no geomagnetic disturbances around the earthquake onset time (Planetary K-Index = 3). GPS satellites of Pseudo Random Noise (PRN) 20, 29, and 05 could capture significant nighttime CIP during this event. Figure 2a shows the ionospheric piercing point (IPP) locations at height of ~350 km for PRN 20 (red), 29 (yellow), and 05 (magenta) at the time of CIP initiation. The locations of the epicenter, *cmbl* and *kaik* GPS sites, are shown in blue star and triangles, respectively.

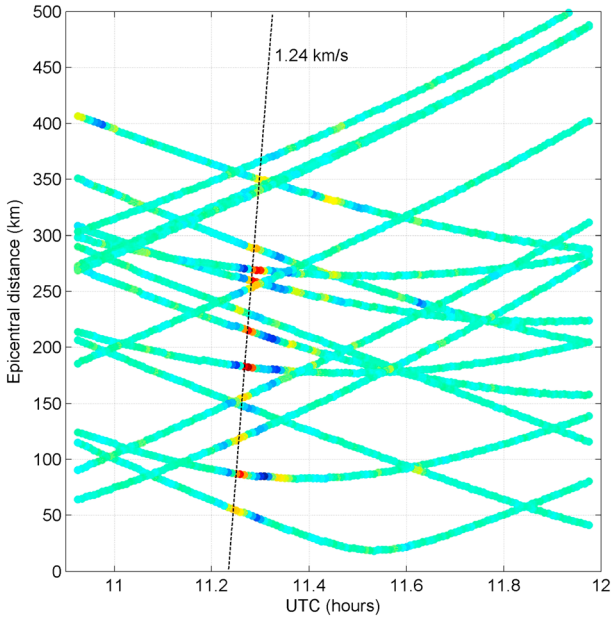

Figure 3. Hodochrone/traveltime showing the velocity estimation performed using CIP distribution in the north of CCTZ. The obtained velocity of ~1.24 km/s emphasizes the acoustic wave as origin of these CIP.

Since TEC is mainly weighted by the maximum electron density in ionosphere, based on International Reference Ionosphere-2012 empirical model at the earthquake local time and epicenter location, an approximate maximum density height of 350 km has been considered as IPP height.

Figure 2b shows CIP as recorded by PRN 20 with elevation >70°. These CIP, observed north of the rupture, exhibit clear N-type TEC variations ~10–15 min within the earthquake onset (red vertical line). The CIP are labeled with the respective observable station names. Significant CIP amplitudes registered at IPP of gldb_20, nlsn_20, cmbl_20, wgtn_20, wrpa_20, dnvk_20, hast_20, wang_20, vgmt_20, and nply_20. Observations by PRN 29 (elevation >65°) (Figure 2c) yield considerable CIP at IPP of nlsn_29, kaik_29, wgtn_29, wrpa_29, and dnvk_29, to the north of the rupture. It is interesting to note that CIP as captured by PRN 20 and 29 toward south and west of rupture exhibit very poor amplitudes. CIP from PRN 05 (elevation between 20° and 25°), which was passing in the eastern side of the rupture, are presented in Figure 2d. N-type CIP registered at IPP of hoki_05, west_05, nlsn_05, gldb_05, and nply_05. PRN 05 observations interestingly suggest that CIP propagated azimuthally in the southeast sector too. The corresponding CIP amplitude and phase became weak with distance.

In order to verify that the observed ionospheric perturbations are of seismic origin, we have compared the detrended TEC time series (cutoff frequency ≤4.8 mHz) for three consecutive days (a day before, the earthquake day, and a day after) recorded by dnvk_20, wrpa_29, and gldb_05 as a test case and shown in Figure S1. It could be noticed that the ionospheric perturbations as observed on the earthquake day are conspicuously absent on other days in all these PRN.

The IPPs of significant CIP are highlighted for each PRN in Figure 2a. The two demarcated clusters of significant CIP in Figure 2a suggest that the CIP preferentially evolved in the north-northeast (observed by PRN 20, 29, and 05) and in east-southeast (observed by PRN 05) of the rupture. Typically, the CIP are linked to the area of maximum coseismic uplift in the vicinity of epicenter (e.g., Astafyeva et al., 2009, 2013, 2011; Astafyeva & Heki, 2009; Heki & Ping, 2005). Moving a step forward, we demonstrate here that the CIP distribution around the epicenter are more related to the rotated surface thrust orientations observed in the direction of rupture. Thus, the multifractured Kaikoura 2016 earthquake event provided very rare opportunity to identify the location(s) of individual seismic source(s) yielding the observed cluster distribution of mid nighttime CIP.

Figure 3 shows the hodochrone/traveltime for the CIP distributed in north of the CCTZ. It could be observed that CIP preferentially propagated with the acoustic velocity of ~1.24 km/s toward north. The obtained velocity demonstrates that the CIP are of acoustic origin during the Kaikoura earthquake. Near similar CIP propagation velocities at ionospheric heights are documented earlier also (e.g., Astafyeva et al., 2009; Sunil et al., 2016). Certainly, the obtained velocity values are slightly higher than the acoustic velocity but lower than the Rayleigh wave induced CIP propagation velocity at the ionospheric *F*-region height. In general, the propagation velocity of Rayleigh wave induced CIP varies ~2.0–4.0 km/s (e.g., Jin et al., 2017; Maruyama et al., 2012).

3. Discussion

Among modern seismological observations, the Kaikoura earthquake of M_w 7.8 is one of the most tectonically complex earthquakes recorded over land (Shi et al., 2017). The coseismic contortion pattern distilled from the above mentioned peculiar ground characteristics (Figures 1b–1d) along the rupture propagation during the Kaikoura event lend support to the complex tectonic environment over the northern region of the South New Zealand Island (Beavan et al., 2002). The focal mechanism (Figure 1a) suggests that the event occurred as a

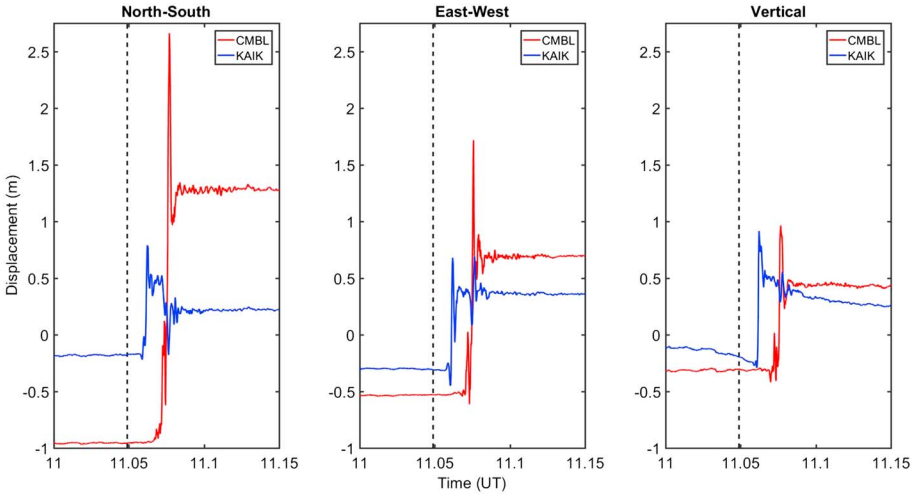

Figure 4. High rate (1 Hz) GPS derived displacement components at sites *cmbl* and *kaik* during the event. The earthquake initiation time is shown with dashed line.

combination of (i) major thrust faulting component due to the convergence between Australian and Pacific plates and (ii) strike-slip faulting due to the presence of right-lateral and left-lateral faults in the northern region of the Southern Island.

The earthquake initiated as a strike-slip rupture with slip toward east, then took a right-lateral and left-lateral slips in the central and northern most part of the rupture, respectively, with the low dip angle oblique thrust (Duputel & Rivera, 2017). Kaiser et al. (2017) and Zhang et al. (2017) reported that from south to north rupture propagation evolved with multi-segments of three to four phases. The GPS vectors (Figure 1b) indeed confirm such a complexity of both, the earthquake and the tectonics of the region. Further, the rupture with diverse source parameters reported by Duputel and Rivera (2017) and Zhang et al. (2017) further corroborate the presence of multiple sources, which control the rupture.

Based on above, the NE oriented (~50° from north) CCTZ and ENE oriented (~80° from north) KCTZ emerge as two possibly distinct seismic sources (Figures 1d and 9) that could disturb the ionosphere and explain the observed unusual CIP disposition. To segregate the contribution of horizontal and vertical displacements toward the resultant thrust orientations at CCTZ and KCTZ, we present high rate (1-Hz) time series of N-S, E-W, and vertical components as measured using GPS at *cmbl* and *kaik* sites in Figure 4. Though the maximum vertical uplift is observed at CCTZ, the large horizontal displacement with major N-S and E-W components at CCTZ has reinforced the thrust mostly toward NE direction. However, at KCTZ, the EW component is more significant, which conveys that thrust is mostly oriented in the EW direction near KCTZ. Yuichiro and Satake (1996) studied two tsunamigenic offshore earthquakes and reported the importance of larger horizontal reinforcement. Additionally, the strike-slip events, which mainly exhibit horizontal displacements, are known to generate CIP as well (e.g., Astafyeva et al., 2014; Cahyadi & Heki, 2015; Sunil et al., 2015).

The disposition of CIP is normally explained invoking surface displacements either at the epicenter or along the rupture as their source (e.g., Astafyeva & Heki, 2009; Heki et al., 2006; Rolland et al., 2013; Sunil et al., 2015, 2016). However, the Kaikoura earthquake rupture constitutes contributions from two thrust zones of CCTZ and KCTZ; the total rupture duration of ~100 s (Zhang et al., 2017) is lower than the characteristic period of acoustic waves (~4 min) in upper atmosphere. Hence, segregation between the tectonic sources of acoustic waves at near-field within rupture duration of ~100 s may not be possible.

We therefore attempt to identify the source(s) that best explain the CIP distribution invoking support of non-tectonic forcing mechanisms such as (i) geomagnetic field-wave coupling, (ii) wave phase cancellation effect due to varying satellite geometry, and (iii) ambient ionization density.

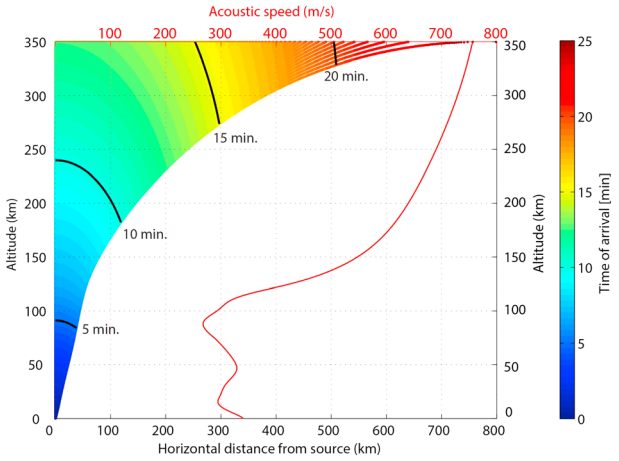

Figure 5. Acoustic raypaths from the CCTZ within 26.75° zenith cutoff estimated based on the refraction of acoustic waves in varying temperature and density media. The color represents the wave arrival time. Sound velocity profile, used to derive acoustic raypaths is also shown.

The seismic induced acoustic wave perturbations impart the momentum energy to the ionospheric plasma through ion-neutral collision. Once the ionospheric density obtains the momentum, it moves along the geomagnetic field lines in the direction of wave velocity perturbation. The coupling efficiency between the geomagnetic field and acoustic wave velocity perturbations could be estimated as $\mathbf{k}.\mathbf{l_b}$ (e.g., George & Hooke, 1970) factor. Here $\mathbf{k}$ is the acoustic wave vector and $\mathbf{l_b}$ is the unit vector in the geomagnetic field direction derived using International Geomagnetic Reference Field-12 model. To derive $\mathbf{k}$, we perform the ray tracing for the seismic induced acoustic waves using wave refraction phenomenon in varying temperature and density media (e.g., Cahyadi & Heki, 2015; Calais et al., 1998; Heki & Ping, 2005), which is discussed in the next para. The geomagnetic field favors the ionospheric plasma movement if acoustic wave perturbations propagate in the direction of the field where the maximum coupling occurs. On the occasion of maximum coupling, the factor equals to a unit value.

Figure 5 shows the acoustic raypaths considering CCTZ as source. The acoustic raypaths in the present study show the propagation direction and the arrival time of the wave at each altitude. The acoustic velocity profile that is used to estimate these raypaths is derived using NRLMSISE-00 model at the location of CCTZ and shown in the figure. The acoustic wave speed varies with the altitudes causing the refraction of rays and changes the wave propagation direction with altitude.

The acoustic rays within around 26.75° zenith angle are observed to propagate further in the ionosphere and rest gets refracted from the lower altitudes. Thus, the geomagnetic field-wave coupling factor is estimated within this zenith angle at 350 km height. The coupling factor is derived separately for the epicenter and CCTZ and shown in Figures 6a and 6b, respectively. As KCTZ is just ~50 km away from the epicenter, the geomagnetic field-wave coupling may not change drastically from that of the epicenter.

The geomagnetic field favors northeast propagation in both of the cases (Figures 6a and 6b). The epicenter location (star), GPS sites *kaik* and *cmbl* (triangles), are shown in the figure. In case the deformation over the epicenter acts as a source, maximum CIP amplitudes would occur at kaik_20, cmbl_20, and wgtn_20 IPP where strong geomagnetic field-wave coupling exists (Figure 6a). This is not the case (Figure 2b). Instead, significant CIP amplitudes are observed at wrpa_20, dnvk_20, and wang_20 IPP (Figure 2b) corroborates that a small deformation over the epicenter (Figure 1b) is an unlikely source to explain the CIP pattern. However,

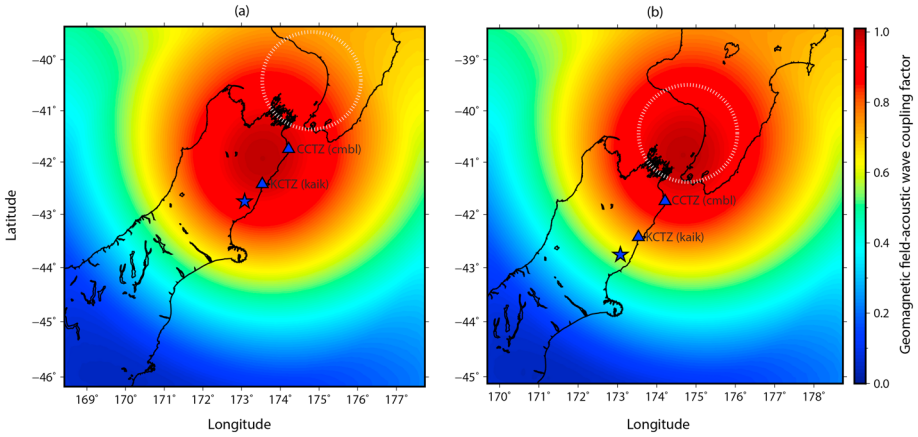

Figure 6. Geomagnetic field-acoustic wave coupling estimated at 350 km height for (a) epicenter and (b) CCTZ. The field is favorable northeast of the respective source. The dashed circle depicts the region where maximum of CIP amplitude occurred.

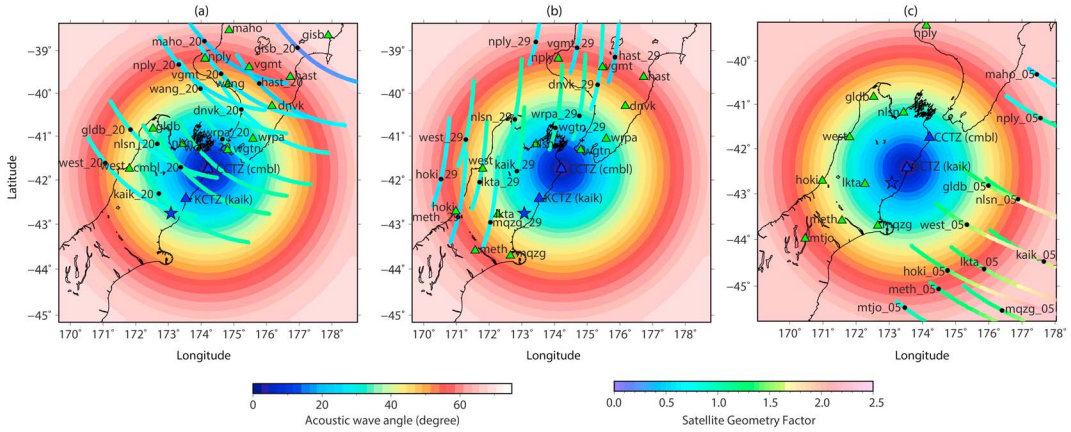

Figure 7. SGF exhibiting the wave phase cancellation effect due to varying satellite geometry. PRN 20 and 29 were passing at high elevation, while PRN 05 was at low elevation at the time of earthquake. (a) SGF estimated for PRN 20 considering CCTZ as the source and shown along the IPP track of PRN 20 from the respective station. (b) Same as Figure 7a but for PRN 29. (c) SGF estimated for PRN 05 considering KCTZ as the source. In case of PRN 05, in southeast sector, the satellite geometry is less supportive. The acoustic wave arrivals in terms of wave angles at 350 km height, estimated using the ray tracing over the respective source for zenith cutoff of ~20°, are also reproduced in the background.

with CCTZ (maximum uplift that reinforced by large north-east horizontal displacement) as a source (Figure 6b), the CIP (Figure 2b) are best explained. Similarly, observations from PRN 29 (Figure 2c) with CCTZ as a source are also well explained. Hence, CIP evolution and propagation toward north of the rupture stands best explained with CCTZ acting as a source.

The wave phase cancellation effects due to varying satellite geometry is also estimated in terms of satellite geometry factor (SGF) (Bagiya et al., 2017; George & Hooke, 1970) for PRN 20 and 29 and presented in Figures 7a and 7b, respectively. The most favorable satellite geometry occurs when wave vector and satellite line of sight are perpendicular to each other. On the other hand, when the acoustic wavefronts and satellite line of sight are perpendicular to each other, the integration of wavefronts cancels the wave phases and thus results into the minimal CIP amplitudes. More details on this could be found in Bagiya et al. (2017). The acoustic wave arrivals in terms of wave angles at 350 km height, as estimated using the ray tracing considering CCTZ as the source, are shown in Figure 7. The SGF with zero values indicates most favorable satellite

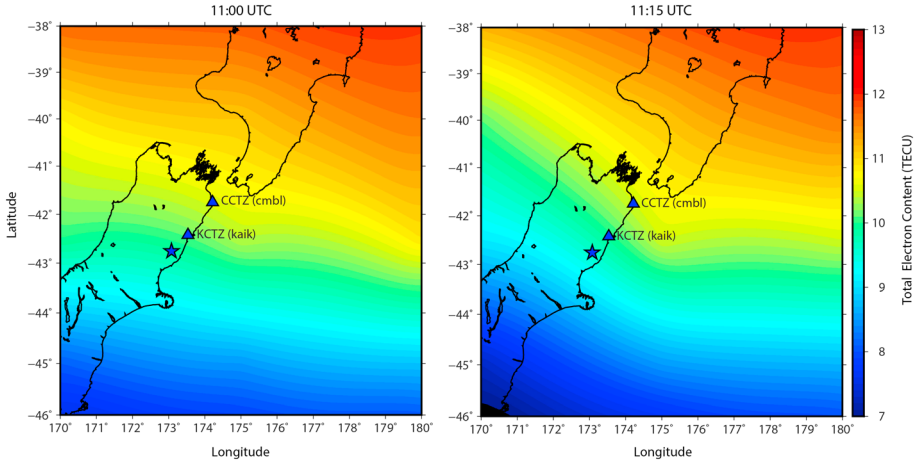

Figure 8. TEC extracted from the global maps by International Global Navigation Satellite Systems Service (a) 11:00 UT and (b) 11:15 UT to evaluate the ambient ionization variability at the time of earthquake.

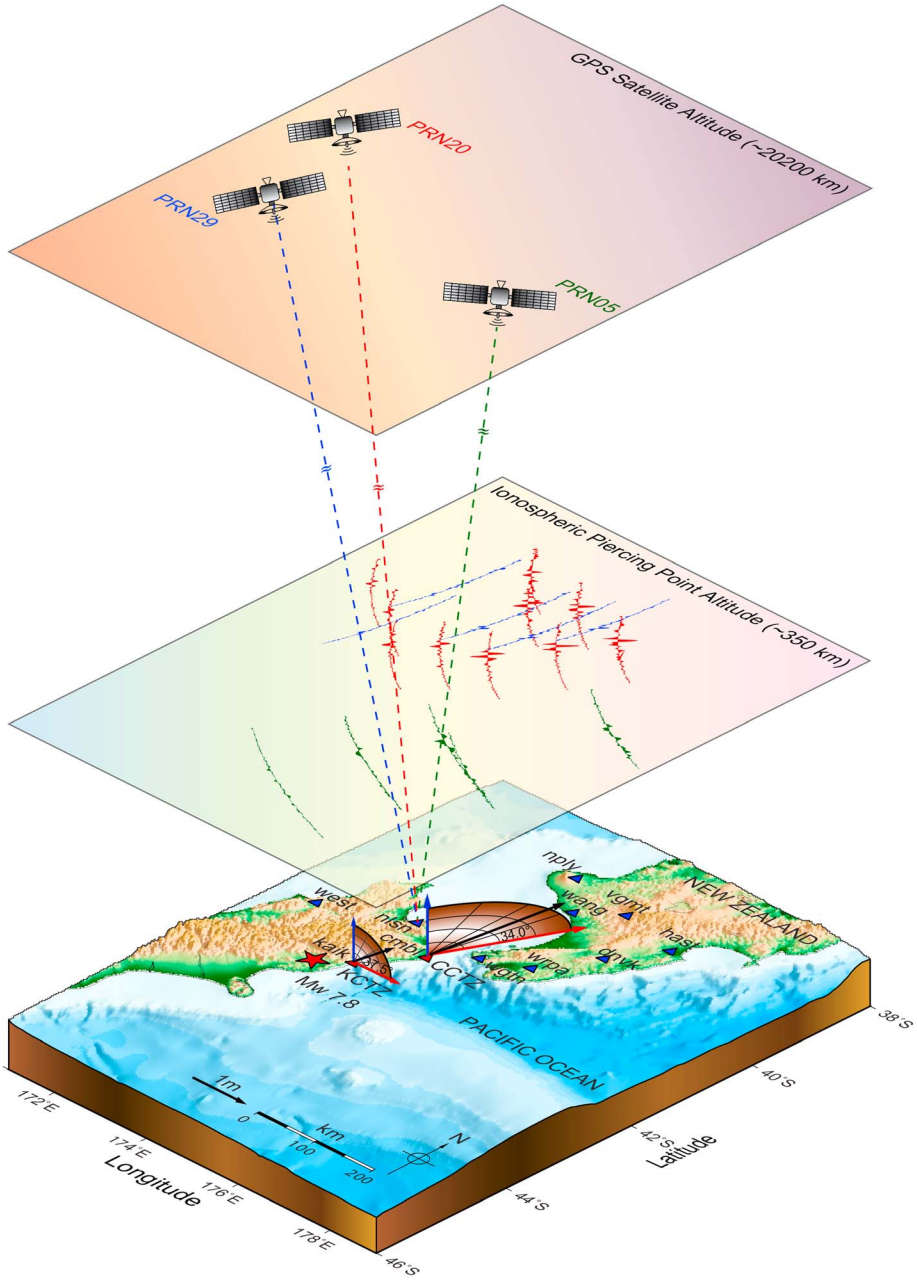

Figure 9. Conceptual 3-D schematic model of the favored mechanism for the origin of CIP disposition delineated from the distinct thrust zones Campbell Coseismic Thrust Zone (CCTZ) and Kaikoura Coseismic Thrust Zone (KCTZ). The bottom slab contains the deformations scenario laid over the topographic map at two demarcated thrust zones KCTZ and CCTZ with horizontal (red arrows) and vertical (blue arrows) displacements. The black arrows represent the resultant thrust angles (37.5° from horizon at KCTZ and 34° from horizon at CCTZ) estimated from the horizontal and vertical displacements. The stereonets depict the total deformed area at two distinct thrust zones. The star and triangles indicate the epicenter of M_w 7.8 event and GPS sites, respectively. The middle plane contains the CIP time series along the satellite IPP tracks for PRN 20 (red), 29 (blue), and 05 (green) at IPP altitude of ~350 km. The topmost horizontal plane contains the respective satellites at orbiting altitude of ~20,200 km. The dashed lines show the representative satellites line of sight from GPS site *nlsn*.

geometry. For PRN 20 the SGF is more favorable further north (Figure 7a). Similarly, in the case of PRN 29, the SGF is favorable on either side of the CCTZ (Figure 7b). Another important observation is complete absence of CIP south of the CCTZ except at kaik_20 (Figure 2b). In case the epicenter was to be the source of the acoustic waves, the CIP over southern parts of CCTZ would be amplified due to favorable geomagnetic field-wave coupling and also favorable SGF (Figures 6b and 7a). However, this is not the case (Figure 6b). It further confirms that the source for CIP in the north is indeed CCTZ.

PRN 05 captured relatively weak CIP in northeast and southeast of the rupture zone compared to amplitudes elsewhere in the earthquake region. As the thrust at CCTZ is mainly NE oriented, PRN 05 CIP cannot be entirely attributed to this source. However, Figure 2a demonstrates that CIP at nply_05 could be due to forcing from CCTZ while the gldb_05 and nlsn_05 contain the contribution from both CCTZ and KCTZ. Nevertheless, we attribute CIP at west_05 and hoki_05 to the source at KCTZ. Incidentally, the thrust at KCTZ is oriented eastward. As mentioned earlier, the KCTZ is just ~50 km away from the epicenter, and hence, it is reasonable to assume that the geomagnetic field-wave coupling remains more or less similar for KCTZ and the epicenter. With this assumption, we state that PRN 05 CIP fall into a weak to moderate geomagnetic field-wave coupling (Figure 6b) region. Also, the phase cancellation effects as estimated from the KCTZ are significant in case of PRN 05 (Figure 7c). Even if SGF is estimated by considering CCTZ as source, the phase cancellation effects would be higher at nply_05, gldb_05, and nlsn_05 due to low elevation of PRN 05.

In addition to the above discussed non tectonic forcing mechanisms, we investigate the contribution from the ambient ionization density in manifesting the observed CIP pattern using GPS derived TEC maps provided by global International GNSS Service. Figure 8 shows the extracted TEC maps at (i) 11:00 UT and (ii) 11:15 UT on the event day. The noticeable feature is the enhancing gentle gradient in ambient ionization toward northeast, which also supports significant CIP in PRN 20 and 29 toward north. On the other hand, weak CIP amplitudes as observed by PRN 05 can be explained through the relatively smaller ambient ionization density in addition to other two less supportive nontectonic forcing. Therefore, the observed weak PRN 05 CIP can be attributed mainly to less supportive nontectonic forcing while tracing their evolution to the NE oriented CCTZ and east oriented KCTZ.

To conceptualize this novel concept, we illustrate the crustal deformations at ground and CIP manifestations at IPP height 350 km along with the viewing satellites at ~20,200 km invoking the 3-D schematic model in Figure 9. The bottom slab demonstrates the deformations scenario over the topographic map at two demarcated distinct thrust zones KCTZ and CCTZ with horizontal (red arrow) and vertical (blue arrow) displacements. The black arrows depict the resultant thrust angles (37.5° from horizon at KCTZ and 34° from horizon at CCTZ) estimated from the horizontal and vertical displacements. The stereonets indicate the total deformed area at two distinct thrust zones. The middle plane contains the CIP time series along the satellite IPP tracks for PRN 20 (red), 29 (blue), and 05 (green) at IPP height of ~350 km. For CIP amplitude scale, please refer to Figure 2. The topmost horizontal plane contains the respective satellites at orbiting heights. The dashed lines show the representative satellite line of sight at GPS site *nlsn*. The role of two distinct surface thrust orientations in controlling the CIP disposition around the deformed area could be clearly and easily visualized from Figure 9.

4. Conclusion

The M_w 7.8 Kaikoura earthquake that occurred in geometrically and tectonically complex environment revealed interesting characteristics from ground based GPS measurements with peculiar manifestations in the ionosphere. Important insights obtained from this study are as follows:

Coseismic GPS vector field suggests that the northeast rupture associated with this event, after nucleation, is influenced by multisegmented slip-distributions arising from two different thrust zones reinforced with major horizontal displacements, which rotated in an anticlockwise direction from the epicenter. The varying thrust zones of CCTZ and KCTZ over the rupture acted as two different sources for CIP. The CIP in north are attributed to CCTZ, while the CIP in NE have contribution from both CCTZ and KCTZ. The CIP in SE are induced by the KCTZ. This CIP disposition is explained by considering the nontectonic forcing mechanisms which strengthen our proposition of tectonic thrust zone orientations as distinct sources, responsible for this peculiar CIP azimuthal propagation.

Acknowledgments
We thank GeoNet (http://geonet.org.nz) and PositioNZ (http://apps.linz.govt.nz/positionz) GNSS networks team for making available the GPS data. The IGS TEC maps are derived from http://cda-web.gsfc.nasa.gov. We thank International Global Navigation Satellite Systems (GNSS) Service Iono Working Group for the same. We acknowledge WDC for Geomagnetism, Kyoto, for providing geomagnetic indices. The figures are prepared by the Generic Mapping Tool (GMT) software (Wessel & Smith, 1996). This work is part of the new interdisciplinary initiative, Lithosphere-Atmosphere-Ionosphere-Magnetosphere (LAIM) coupling program, of the Indian Institute of Geomagnetism (DST), Navi Mumbai, India. A.S. duly acknowledges the DST, India, for providing research fellowship. We thank the reviewers for providing constructive suggestions.

References

Astafyeva, E., & Heki, K. (2009). Dependence of waveform of near-field coseismic ionospheric disturbances, on focal mechanisms. *Earth, Planets and Space*, *61*(7), 939–943. https://doi.org/10.1186/BF03353206

Astafyeva, E., Heki, K., Kiryushkin, V., Afraimovich, E., & Shalimov, S. (2009). Two-mode long-distance propagation of coseismic ionosphere disturbances. *Journal of Geophysical Research*, *114*, A10307. https://doi.org/10.1029/2008JA013853

Astafyeva, E., Lognonné, P., & Rolland, L. (2011). First ionosphere images for the seismic slip of the Tohoku-oki earthquake. *Geophysical Research Letters*, *38*, L22104. https://doi.org/10.1029/2011GL049623

Astafyeva, E., Rolland, L., Lognonné, P., Khelfi, K., & Yahag, T. (2013). Parameters of seismic source as deduced from 1 Hz ionospheric GPS data: Case study of the 2011 Tohoku-oki event. *Journal of Geophysical Research: Space Physics*, *118*, 5942–5950. https://doi.org/10.1002/jgra.50556

Astafyeva, E., Rolland, L. M., & Sladen, A. (2014). Strike-slip earthquakes can also be detected in the ionosphere. *Earth and Planetary Science Letters*, *405*, 180–193.

Bagiya, M. S., Sunil, A. S., Sunil, P. S., Sreejith, K. M., Rolland, L., & Ramesh, D. S. (2017). Efficiency of coseismic ionospheric perturbations in identifying crustal deformation pattern: Case study based on M_w 7.3 May Nepal 2015 arthquake. *Journal of Geophysical Research: Space Physics*, *122*, 6849–6857. https://doi.org/10.1002/2017JA024050

Beavan, J., Tregoning, P., Bevis, M., Kato, T., & Meertens, C. (2002). Motion and rigidity of the Pacific Plate and implications for plate boundary deformation. *Journal of Geophysical Research*, *107*(B10), 2261. https://doi.org/10.1029/%202001JB000282

Cahyadi, M. N., & Heki, K. (2015). Coseismic ionospheric disturbance of the large strike-slip earthquakes in North Sumatra in 2012: M_w dependence of the disturbance amplitudes. *Geophysical Journal International*, *200*(2015), 116–129.

Calais, E., Minster, J. B., Hofton, M. A., & Hedlin, M. A. H. (1998). Ionospheric signature of surface mine blasts from Global Positioning System measurements. *Geophysical Journal International*, *132*, 191–202.

Duputel, Z., & Rivera, L. (2017). Long-period analysis of the 2016 Kaikoura earthquake. *Physics of the Earth and Planetary Interiors*, *265*, 62–66. https://doi.org/10.1016/j.pepi.2017.02.004

George, T. M., & Hooke, W. H. (1970). Wave-induced fluctuations in ionospheric electron content—A model indicating some observational biases. *Journal of Geophysical Research*, *75*(31), 6295–6308. https://doi.org/10.1029/JA075i031p06295

Hamling, I. J., Hreinsdóttir, S., Clark, K., Elliott, J., Liang, C., Fielding, E., et al. (2017). Complex multifault rupture during the2016 M_w 7.8 Kaikoura earthquake, New Zealand. *Science*, *356*(6334), eaam7194. https://doi.org/10.1126/science.aam7194

Heki, K., & Ping, J. (2005). Directivity and apparent velocity of the coseismic ionospheric 348 disturbances observed with a dense GPS array. *Earth and Planetary Science Letters*, *236*(349), 845–855. https://doi.org/10.1016/j.epsl.2005.06.010

Heki, K., Otsuka, Y., Choosakul, N., Hemmakorn, N., Komolmis, T., & Maruyama, T. (2006). Detection of ruptures of Andaman fault segments in the 2004 great Sumatra earthquake with coseismic ionospheric disturbances. *Journal of Geophysical Research*, *111*, B09313. https://doi.org/10.1029/2005JB004202

Jin, S., Jin, R., & Li, D. (2017). GPS detection of ionospheric Rayleigh wave and its source following the 2012 Haida Gwaii earthquake. *Journal of Geophysical Research: Space Physics*, *122*, 1360–1372. https://doi.org/10.1002/2016JA023727

Kaiser, A., Balfour, N., Fry, B., Holden, C., Litchfield, N., Gerstenberger, M., et al. (2017). The 2016 Kaikoura, New Zealand, Earthquake: Preliminary Seimologicla Report. *Seismological Research Letters*, *88*(3), 727–739. https://doi.org/10.1785/0220170018

Maruyama, T., Tsugawa, T., Kato, H., Ishii, M., & Nishioka, M. (2012). Rayleigh wave signature in ionograms induced by strong earthquakes. *Journal of Geophysical Research*, *117*, A08306. https://doi.org/10.1029/2012JA017952

Rolland, L. M., Vergnolle, M., Nocquet, J. M., Sladen, A., Dessa, J. X., Tavakoli, F., et al. (2013). Discriminating the tectonic and non-tectonic contributions in the ionospheric signature of the 2011, M_w7.1, dip-slip Van earthquake, Eastern Turkey. *Geophysical Research Letters*, *40*, 2518–2522. https://doi.org/10.1002/grl.50544

Shi, X., Wang, Y., Liu-Zeng, J., Weldon, R., Wei, S., Wang, T., & Sieh, K. (2017). How complex is the 2016 M_w 7.8 Kaikoura earthquake, South Island, New Zealand? *Scientific Bulletin*, *62*, 309–311. https://doi.org/10.1016/j.scib.2017.01.033

Sunil, A. S., Bagiya, M. S., Reddy, C. D., Kumar, M., & Ramesh, D. S. (2015). Post-seismic ionospheric response to the 11 April 2012 East Indian Ocean doublet earthquake. *Earth, Planets and Space*, *67*(1), 37. https://doi.org/10.1186/s40623-015-0200-8

Sunil, A. S., Bagiya, M. S., Catherine, J., Rolland, L., Sharma, N., Sunil, P. S., & Ramesh, D. S. (2016). Dependence of near field co-seismic ionospheric perturbations on surface deformations: A case study based on the April, 25 2015 Gorkha Nepal earthquake. *Advances in Space Research*, *59*(5), 1200–1208. https://doi.org/10.1016/j.asr.2016.11.041

Wessel, P., & Smith, W. H. F. (1996). New version of Generic Mapping Tool released. *Eos, Transactions American Geophysical Union*, *F76*, 329.

Williams, S. D. P., Bock, Y., Fang, P., Jamason, P., Nikolaidis, R. M., Prawirodirdjo, L., et al. (2004). Error analysis of continuous GPS position time series. *Journal of Geophysical Research*, *109*, B03412. https://doi.org/10.1029/2003JB002741

Yuichiro, T., & Satake, K. (1996). Tsunami generation by horizontal displacement of ocean bottom. *Geophysical Research Letters*, *23*(8), 861–864.

Zhang, H., Koper, K. D., Pankow, K., & Ge, Z. (2017). Imaging the 2016 M_w 7.8 Kaikoura, New Zealand earthquake with teleseismic *P* waves: A cascading rupture across multiple faults. *Geophysical Research Letters*, *44*, 4790–4798. https://doi.org/10.1002/2017GL073461